On-chip optical trapping and Raman spectroscopy using a TripleX dual-waveguide trap

Martijn Boerkamp,[1] Thijs van Leest,[1,2] Jeroen Heldens,[1,2] Arne Leinse,[3] Marcel Hoekman,[3] Rene Heideman,[3] and Jacob Caro[1*]

[1]*Department of Imaging Physics, Delft University of Technology, Lorentzweg 1, 2628 CJ Delft, The Netherlands*
[2]*Kavli Institute of Nanoscience Delft, Delft University of Technology, Lorentzweg 1, 2628 CJ Delft, The Netherlands*
[3]*Lionix B.V., PO Box 456, Enschede, The Netherlands*
[*]*j.caro@tudelft.nl*

Abstract: We present a new approach to the dual-beam geometry for on-chip optical trapping and Raman spectroscopy, using waveguides microfabricated in TripleX technology. Such waveguides are box shaped and consist of SiO_2 and Si_3N_4, so as to provide a low index contrast with respect to the SiO_2 claddings and low loss, while retaining the advantages of Si_3N_4. The waveguides enable both the trapping and Raman functionality with the same dual beams. Polystyrene beads of 1 μm diameter can be easily trapped with the device. In the axial direction discrete trapping positions occur, owing to the intensity pattern of the interfering beams. Trapping events are interpreted on the basis of simulated optical fields and calculated optical forces. The average transverse trap stiffness is 0.8 pN/nm/W, indicating that a strong trap is formed by the beams emitted by the waveguides. Finally, we measure Raman spectra of trapped beads for short integration times (down to 0.25 s), which is very promising for Raman spectroscopy of microbiological cells.

©2014 Optical Society of America

OCIS codes: (140.7010) Laser trapping; (170.5660) Raman spectroscopy; (230.3120) Integrated optics devices; (230.7390) Waveguides, planar.

References and links

1. M. B. Fenn, V. Pappu, P. G. Georgeiv, and P. M. Pardalos, "Raman spectroscopy utilizing Fisher-based feature selection combined with support vector machines for the characterization of breast cell lines," J. Raman Spectrosc. **44**(7), 939–948 (2013).
2. J. van de Vossenberg, H. Tervahauta, K. Maquelin, C. H. W. Blokker-Koopmans, M. Uytewaal-Aarts, D. van der Kooij, A. P. van Wezel, and B. van der Gaag, "Identification of bacteria in drinking water with Raman spectroscopy," Anal. Methods **5**(11), 2679–2687 (2013).
3. Z. Movasaghi, S. Rehman, and I. U. Rehman, "Raman spectroscopy of biological tissues," Appl. Spectrosc. Rev. **42**(5), 493–541 (2007).
4. C. Xie, J. Mace, M. A. Dinno, Y. Q. Li, W. Tang, R. J. Newton, and P. J. Gemperline, "Identification of single bacterial cells in aqueous solution using confocal laser tweezers Raman spectroscopy," Anal. Chem. **77**(14), 4390–4397 (2005).
5. J. W. Chan, "Recent advances in laser tweezers Raman spectroscopy (LTRS) for label-free analysis of single cells," J Biophotonics **6**(1), 36–48 (2013).
6. S. Mandal, X. Serey, and D. Erickson, "Nanomanipulation using silicon photonic crystal resonators," Nano Lett. **10**(1), 99–104 (2010).
7. T. van Leest and J. Caro, "Cavity-enhanced optical trapping of bacteria using a silicon photonic crystal," Lab Chip **13**(22), 4358–4365 (2013).
8. H. Sumikura, E. Kuramochi, H. Taniyama, and M. Notomi, "Cavity-enhanced Raman scattering of single-walled carbon nanotubes," Appl. Phys. Lett. **102**(23), 231110 (2013).
9. P. R. T. Jess, V. Garcés-Chávez, D. Smith, M. Mazilu, L. Paterson, A. Riches, C. S. Herrington, W. Sibbett, and K. Dholakia, "Dual beam fibre trap for Raman micro-spectroscopy of single cells," Opt. Express **14**(12), 5779–5791 (2006).

10. T. van Leest, F. Bernal Arango, and J. Caro, "Optical forces and trapping potentials of a dual-waveguide trap based on multimode solid-core waveguides," J. Eur. Opt. Soc-Rapid. **6**, 110221 (2011).
11. K. C. Neuman and S. M. Block, "Optical trapping," Rev. Sci. Instrum. **75**(9), 2787–2809 (2004).
12. I. Bloch, "Ultracold quantum gases in optical lattices," Nat. Phys. **1**(1), 23–30 (2005).
13. S. Dochow, C. Krafft, U. Neugebauer, T. Bocklitz, T. Henkel, G. Mayer, J. Albert, and J. Popp, "Tumour cell identification by means of Raman spectroscopy in combination with optical traps and microfluidic environments," Lab Chip **11**(8), 1484–1490 (2011).
14. S. Dochow, M. Becker, R. Spittel, C. Beleites, S. Stanca, I. Latka, K. Schuster, J. Kobelke, S. Unger, T. Henkel, G. Mayer, J. Albert, M. Rothhardt, C. Krafft, and J. Popp, "Raman-on-chip device and detection fibres with fibre Bragg grating for analysis of solutions and particles," Lab Chip **13**(6), 1109–1113 (2013).
15. O. G. Hellesø, P. Løvhaugen, A. Z. Subramanian, J. S. Wilkinson, and B. S. Ahluwalia, "Surface transport and stable trapping of particles and cells by an optical waveguide loop," Lab Chip **12**(18), 3436–3440 (2012).
16. P. Løvhaugen, B. S. Ahluwalia, T. R. Huser, and O. G. Hellesø, "Serial Raman spectroscopy of particles trapped on a waveguide," Opt. Express **21**(3), 2964–2970 (2013).
17. TriPleX^{TM}is a trademark for LioniX's waveguide technology.
18. A. Leinse, R. Heideman, M. Hoekman, C. Bruinink, C. Roeloffzen, L. Zhuang, D. Marpaung, and M. Burla, "TriPleX photonic platform technology: Low-loss waveguide platform for applications from UV to IR," in *Proceedings of the 16th European Conference on Integrated Optics*, ECIO 2012, 1–2 (2012).
19. R. Heideman, M. Hoekman, and E. Schreuder, "TriPleX-based integrated optical ring resonators for lab-on-a-chip and environmental detection," IEEE J. Sel. Top. Quantum Electron. **18**(5), 1583–1596 (2012).
20. Lumerical FDTD Solutions, Inc., *http://www.lumerical.com/tcad-products/fdtd/* (accessed Nov. 14, 2014).
21. B. Jasse, R. S. Chao, and J. L. Koenig, "Laser Raman scattering in uniaxially oriented atactic polystyrene," J. Polym. Sci., Polym. Phys. Ed. **16**(12), 2157–2169 (1978).
22. K. J. Thomas, M. Sheeba, V. P. N. Nampoori, C. P. G. Vallabhan, and P. Radhakrishnan, "Raman spectra of polymethyl methacrylate optical fibres excited by a 532 nm diode pumped solid state laser," J. Opt. A, Pure Appl. Opt. **10**(5), 055303 (2008).

1. Introduction

Today's strong interest in characterization of biological samples with optical methods has initiated several research directions, including classification and identification of biological cells with Raman spectroscopy [1,2]. With this technique, which comprises the spectral analysis of photons inelastically scattered by a sample placed in a region of highly concentrated monochromatic light, vibrations of the constituent molecules are probed to yield the sample's chemical fingerprint [3]. In Raman *tweezers* spectroscopy, a laser-beam focus for inducing a Raman signal from a microscopic particle in a fluid also serves to immobilize the particle by optical trapping [4,5], so as to enable building up a sufficient signal-to-noise ratio in the Raman spectrum. In this way one can first select *e.g.* a biological cell by trapping and then perform Raman spectroscopy on it. These functionalities can be transferred to a lab-on-a-chip situation using a photonic crystal with a cavity [6–8] or a dual-beam trap [9].

In this context, a very attractive approach is the dual-*waveguide* trap [10]. In this device *microfabricated optical waveguides*, from which counter-propagating beams emanate, replace the *optical fibres* [9] of the dual-beam trap in creating the strong light concentration for on-chip trapping and Raman spectroscopy. In [10] we characterize this new design in a simulation study of the optical forces and trapping potentials. Trapping is described as resulting from a force directed transverse and a force directed parallel to the beams, together determining the particle's position in the trap. A salient difference with conventional optical tweezers [11] is that for a dual-waveguide trap with coherently excited modes in either waveguide, the force in the direction parallel to the beams is oscillatory as a result of beam interference [10]. This gives rise to multiple stable trapping positions, a situation similar to that of optical lattices used to study trapped atoms [12].

Dual-beam optical traps have recently been further developed [13–16]. High quality fibre-based traps have been demonstrated, applying fibres solely for trapping [13], and for trapping, Raman excitation and signal collection [14]. However, in view of the delicate mounting of the fibres, this approach does not permit widespread use. The trap reported in [15,16] is based on microfabricated Ta_2O_5 waveguides. Although this is a very important step forward in view of the fabrication procedure, the research material Ta_2O_5 is not likely to give rise to a general

waveguiding platform for sensing. In addition, the Ta_2O_5 waveguides are reported to be lossy [15], thus requiring an additional Raman excitation laser.

Here, we report on a dual-*waveguide* trapping and Raman device fabricated in TripleX waveguide technology [17–19], of the monolithic design we proposed in [10]. The box shaped waveguides produced in this technology (section 2) consist of layers of low-loss SiO_2 and Si_3N_4, so as to obtain a low index contrast with respect to the SiO_2 cladding, while retaining the advantages of Si_3N_4. A further property of the waveguides is the low birefringence. The integrated photonics platform based on these waveguides is compatible with CMOS technology, thus automatically fulfilling the requirement for mass fabrication of the device we study here. The waveguides are highly transparent in the very wide wavelength range 405-2350 nm, similar to Si_3N_4 waveguides, but contrary to silicon-on-insulator, InP and Ta_2O_5. Therefore, the waveguides can be used at $\lambda = 785$ nm, a standard Raman excitation wavelength, making an additional Raman laser as in [15] redundant. The waveguides used here are to be preferred over Si_3N_4 waveguides because of the low effective index (section 3), which gives beam profiles favourable for trapping and Raman spectroscopy. With our device we successfully trap polystyrene beads and induce a clear Raman effect in the trapped beads.
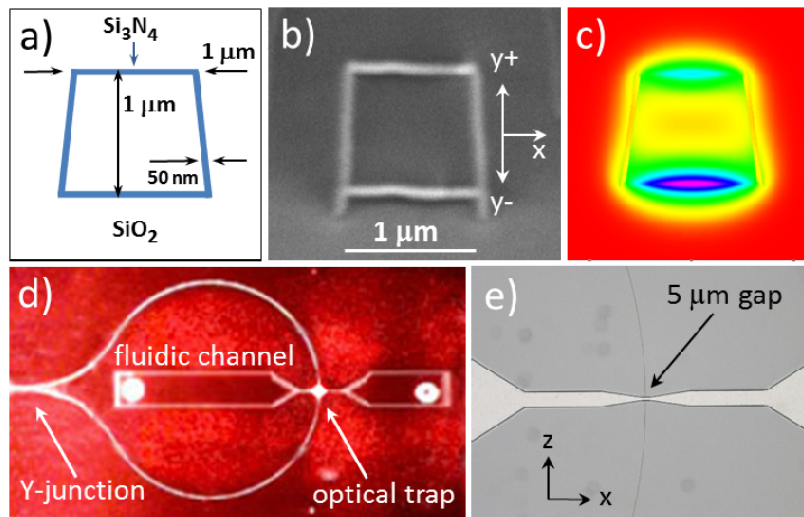

Fig. 1. (a) Cross-sectional schematic with dimensions and materials of the waveguide. The blue trapezoidal box shape is Si_3N_4. Both the inner region of the box and the surrounding cladding are SiO_2. (b) Cross-sectional SEM picture of a waveguide with the box structure. (c) Mode profile of the lowest TE mode in the waveguide, represented as P_z, the z-component of the Poynting vector. Colours from purple to red indicate increasing values of P_z. (d) Microscope image of the Raman trapping device taken while red light was coupled into the input waveguide to check waveguide continuity, giving the red glow. A 50/50 Y-junction splits the input waveguide in two half-circular arms (circle diameter = 7 mm), which guide the light to the fluidic channel. The waveguiding structures are imaged as white due to saturation of the camera. For clarity, white saturation regions due to scattering loss at the input waveguide and at the trap have been removed. (e) Microscope image of the central region of the device. Each of the two waveguides terminates in a wall of the 5 μm wide fluidic channel, which tapers up in two steps. Definition of the coordinate axes as indicated in b) and e).

2. Design of the dual-waveguide trap and experimental setup

A cross-sectional schematic of the waveguides is shown in Fig. 1(a). The waveguide has a slightly trapezoidal box shape. The width at the base and the top of the box are 1.1 and 1.0 μm, respectively, while its height is 1.0 μm. The wall of the box is 50 nm thick Si_3N_4. Both the material of the inner region and the surrounding cladding of the box are SiO_2. A cross-sectional scanning electron microscope image of a waveguide is given in Fig. 1(b), along with the mode profile of the lowest order TE mode in Fig. 1(c). The profile for this polarization

clearly shows the tendency to concentrate the field in the horizontal walls of the box, as expected for higher index regions.

The device is fabricated as an assembly of a waveguide, a 50/50 Y-junction and a loop, as can be seen in Fig. 1(d). To create the trapping geometry, a gap is opened in the loop by dry etching successively through the upper cladding (12 µm SiO_2), the waveguide and the lower cladding (8 µm SiO_2). In this way an integrated fluidic channel and two faceted waveguides, from which counter-propagating beams are launched into the channel, are formed in a single step. The devices are sealed by bonding a glass wafer onto the device wafer, with pre-etched holes for access to the fluidic channel of each device. The final step is dicing, which produces a sufficient quality facet of the input waveguide of a device for incoupling of light.

The narrowest section of the channel, located between the waveguides, is 5 µm wide and 20 µm long. Outside this section, the channel tapers up to 1 mm wide in two steps (Fig. 1(e)). The coordinate system we use in the following sections is defined by taking x parallel to the fluidic channel axis, y in the vertical direction and z along the waveguide axes (see Fig. 1(b),1(e)), the trap centre being the origin of the coordinate system.

A schematic of the experimental setup is shown in Fig. 2. The light source of the system is a Sacher Raman laser operating at 785 nm. The light path to the chip includes a laser clean-up filter, a laser-to-fibre coupler and a polarization maintaining single mode fibre. The fibre is butt-coupled to the input waveguide of the device using a high resolution xyz piezo stage, so as to enable optimum excitation of the waveguide's lowest TE mode.
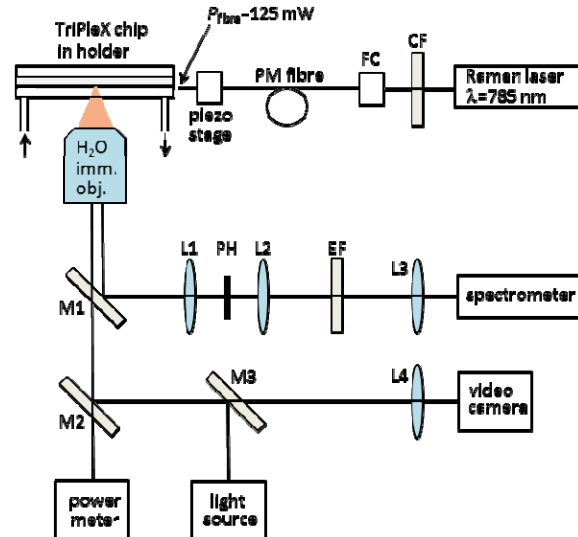

Fig. 2. Schematic of the setup for optical trapping and Raman spectroscopy with the dual-waveguide trap, which is clamped in a holder with ports for fluidic access. Components: CF – laser clean-up filter, FC – fibre coupler, M1, M2 – dichroic mirrors, M3 – beam splitter, L1, PH, L2 – lenses and pinhole of confocal filter, EF – razor edge filter, L3, L4 – aperture matching lens and imaging lens for spectrometer and camera, respectively. In most of the experiments, the power offered by the fibre to the input waveguide was 125 mW, as indicated.

Raman scattered photons generated in a trapped particle are collected by a water immersion objective (NA = 0.80) and directed to a Princeton Instruments LS 785 spectrometer (resolution 5 cm^{-1}) via a dichroic mirror, a confocal filter (pin-hole size 200 µm), a razor-edge filter and a lens focusing the signal on the spectrometer's slit. Finally, there are light paths for visual inspection and monitoring of the trapped particle(s) and to follow alignment of the fibre to the waveguide, and for measurement of light scattered elastically

from the empty trap. For this a LED light source, a beam splitter, a camera and a power meter are included (see Fig. 2).

The chip is mounted in a holder comprising a pair of Perspex plates, of which the lower plate has a thickness matching with the objective's working distance of 3.3 mm and which has O-ring seals to the access holes in the chip. The holder, in turn, is mounted on an xy-translation stage. The objective has z-translation. Water with dispersed polystyrene beads is loaded into the fluidic channel from a motorized syringe pump, connected to the holder via peek tubing. Water flow velocities for the experiments, in the range 7-90 µm/s, are obtained by stabilizing the flow without pump activity.

3. Optical field of the dual-waveguide trap

To characterize the optical field of the device we performed finite-difference time-domain (FDTD) simulations using Lumerical software [20]. In each waveguide the lowest TE mode for $\lambda = 785$ nm is excited. In the simulations coherent modes thus propagate towards the end facets of the waveguides, together delivering 1.0 W of power to the trap. Simulated patterns of the time-averaged intensity of the electric field, both for the xz-plane and the yz-plane, are shown in Fig. 3.

In this figure, the intensity pattern between the waveguides and inside the waveguides is characterized by standing wave modulation due to beam interference. In the gap between the waveguides the period deduced from the modulation amounts to 299 nm, in close agreement with the expected value $\lambda_{H2O}/2 = 785$ nm/$(2 \times 1.33) = 295$ nm ($n_{H2O} = 1.33$). The period of the oscillations in the waveguides is some smaller than in the gap, due to their higher index ($n_{eff} = 1.49$ @ $\lambda = 785$ nm). The clear presence of the interference pattern inside the waveguides indicates that an appreciable fraction of each emitted beam is transmitted into the opposite waveguide, as a result of the low index contrast between the waveguides and water.

For the high field region of the patterns near the optical axis and in the gap, only weak beam spreading is observed, whereas near the facets this region clearly differs for the two cross-sectional planes. This weak spreading is in contrast to the rather strong spreading found for homogeneous Si_3N_4 waveguides [10]. This difference arises from the lower index contrast of the waveguides with respect to water as compared to that of Si_3N_4 waveguides with respect to water (in [10] $n_{Si3N4} = 1.9$), resulting in weaker confinement of the guided mode and less diffraction at the waveguide facets.
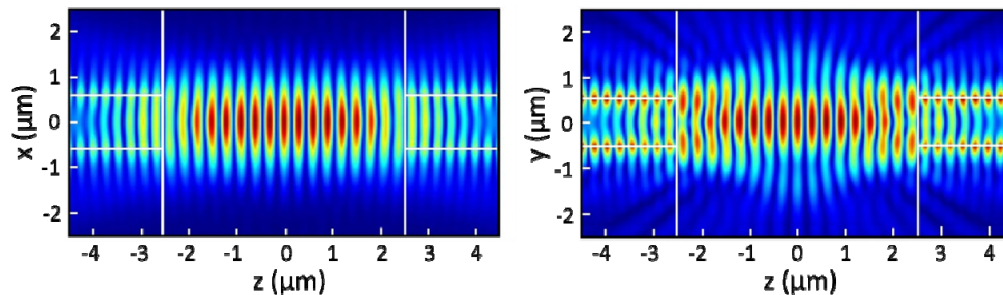

Fig. 3. Simulated patterns of the intensity of the electric field in (a) the xz-plane and (b) the yz-plane. The pattern results from excitation of the lowest TE mode and shows standing wave modulation due to beam interference. The polarization is in the x-direction.

In the yz-plane, going from guided mode to radiation mode, the profile evolves in a way characteristic of this type of composite oxide/nitride waveguide. In the waveguide the modal profile has lobes concentrated in the Si_3N_4 walls of the box, which is energetically favourable in view of the polarization being parallel to these walls (*i.e.* perpendicular to the yz-plane). Outside the waveguide the lobes merge to form a more regular pattern, of which the central high field region is slightly narrower than the corresponding region in the xz-plane. In the xz-

plane the profile's evolution from guided to radiation mode is smoother, which relates to the polarization now being perpendicular to the walls (i.e. in the xz-plane).

Details of the highly concentrated optical field in the gap between the waveguides determine several aspects of the optical force characteristics of the device, as discussed in the next section.

4. Trapping experiments

We clearly observe optical trapping of single polystyrene beads upon their delivery by the flow to the trapping region between the waveguides. A single bead can be kept in the trap for a long time (> 10 min.), provided it does not undergo a head-on collision with another arriving bead, which then may take its place. While being trapped, the bead shows Brownian motion in the optical confinement potential of the trap. When the supply of light to the trap is stopped, the bead is released into the flow. The trap is strong enough to trap more than a single bead, as may be seen in various trapping events recorded in the supplementary Media 1 and Media 2. Snapshots of these media are presented in the three panels of Fig. 4, showing one bead in the trap, and two different configurations of five and four beads in the trap. For these trapping events the optical power presented to the input waveguide by the fibre was 125 mW. In Media 1 and Media 2 we further observe that a bead can become trapped at various discrete paraxial positions between the waveguides, depending on where it arrives, and that it subsequently may hop to c.q. between what appear to be preferential positions. When several beads are trapped, they may assemble into a lump or into a short chain located on the z-axis (see Fig. 2(b), 2(c)). Assembly of multiple beads in the trap and the related changing configurations can be followed in Media 2.
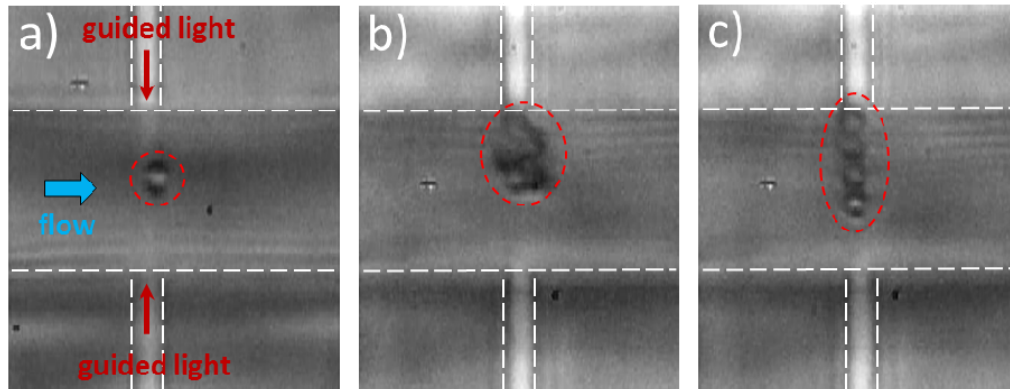

Fig. 4. Snapshots (a) and (b, c) of the online supplementary Media 1 and Media 2, respectively. A single trapped bead can be seen in a). In b) and c) a lump a five trapped beads and a linear chain of four trapped beads are shown, respectively. The respective water flow velocities for the panels are 90, 34 and 43 μm/s. Dashed lines indicate the boundaries of the fluidic channel and the dual waveguides.

5. Force calculations and optical power considerations

To calculate the optical forces $F_x(x)$, $F_y(y)$ and $F_z(z)$ in the three directions, we use the electromagnetic fields derived from FDTD simulations, with the bead in position, as input data for the Maxwell stress-tensor method. The mesh sizes used in the bead, the waveguides and the remaining FDTD volume are 5, 10 and 30 nm, respectively. The refractive index used for Si_3N_4, SiO_2 and polystyrene are 2.00, 1.45 and 1.58, respectively. In the simulations the bead position is varied on the x-, y- and z-axis. In view of symmetry, we only use half-axes for the x- and z-direction, but use the full y-axis to study the effect of the asymmetry of the box shape (using the half-axes y+ and y-; see Fig. 1(b)). The results are presented in Fig. 5.

The transverse forces F_x and $F_{y+(-)}$ in Fig. 5 show the typical restoring behaviour of the gradient force: upon displacement from the trap centre the force pulls the bead back. Further, with increasing displacement the force goes through an extremum, the position of which marks the point beyond which the effective gradient of the field intensity probed by the bead decreases. As for the magnitude of $F_{y+(-)}$ and the position of their extrema, small but discernible differences occur with respect to these quantities of F_x. In particular, the extrema of $F_{y+(-)}$ slightly exceed the extremum of F_x, and occur for smaller displacement than for F_x, whereas for displacements below 0.5 μm the magnitudes of $F_{y+(-)}$ exceed that of F_x. Such properties can be understood from details of the field distribution in Fig. 3. For example, for small displacements the gradient of the field intensity turns out to be stronger for direction $y+$ than for direction $y-$, while this difference becomes negligible for larger displacements. This agrees with the calculated force behaviour. For larger displacements in the x-direction the intensity gradient exceeds the gradient for either y-directions, leading to the larger calculated forces for that range.

From the initial slope of the force curves we determine transverse trap stiffnesses of 0.73 and 0.87 pN/nm/W for the x- and y-direction, respectively (taking the average for y+ and y-). These values amply exceed, by a factor ≈25, those for the dual-waveguide trap in [10] based on homogeneous Si_3N_4 waveguides. This is due to the weaker beam spreading in the trap, giving stronger transverse gradients. The values also exceed those of conventional optical tweezers, for which a few tenths of pN/nm/W are reported for the transverse case [11]. It follows that this trap is a strong trap.
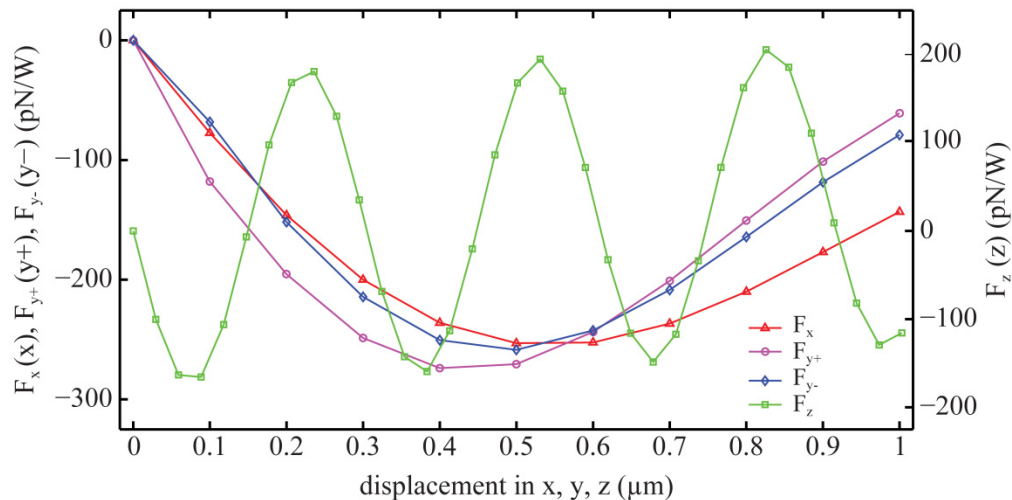

Fig. 5. Calculated forces F_x, $F_{y+ (-)}$ and F_z for displacement of a 1 μm polystyrene bead on the three corresponding axes. The axes y+ (y-) are defined in Fig. 1b.

The axial force F_z in Fig. 5 oscillates strongly around zero, with the same period as the intensity modulation in Fig. 3. The oscillatory force thus reflects the beam interference. Multiple points of stable trapping exist on the periodic curve, characterized by $F_z = 0$ and a negative slope, *i.e.* for $x = m \times \lambda/(2n_{H20}) = m \times 295$ nm ($m = 0,1,2,…$), the positions of the interference maxima. Such multiple stable points agree with the experimental observation of several discrete axial trapping positions and hopping between these, discussed in the previous section and illustrated in Media 1. The trap stiffness for F_z related to a stable point equals the slope at a zero crossing of an oscillation, and amounts to 3.8 pN/nm/W. This value characterizes very strong local traps in the z-direction. The envelope of the oscillations has a slight positive slope. This corresponds to a weak force towards the waveguide facets, contrary to the usual direction of the scattering force for divergent dual beams. We explain this as

resulting from the characteristics of the radiation mode emitted by this type of waveguide, in particular to the merging of the lobes as discussed in relation to Fig. 3(b).

The optical power supplied to the trap (P_{trap}), a key figure of merit, cannot be measured directly. Therefore, we derive P_{trap} from release experiments. In such experiments P_{trap} is lowered by lowering P_{fibre}, the power offered by the fibre, to the value where F_x is just not balanced by the drag force F_d exerted on the bead by the flow. This leads to the bead's release into the flow. At release F_x to a good approximation equals $F_d = 6\pi\eta r v$. Here $\eta = 10^{-3}$ Pa.s is the dynamic viscosity of water, r the bead radius and v the water velocity at release. The water velocity equals the bead velocity immediately after release, which we deduce from the bead position in successive frames of the movie of the release event. The resulting F_x values at release for the various water-flow velocities, which in these experiments take values up to 0.6 pN, correspond to the extremum of $F_x(x)$ in Fig. 5 (250 pN/W) and thus yield the related P_{trap} values, which are found to range up to 2.4 mW.

Release experiments also yield the relation between P_{trap} and P_{fibre}. We obtain this relation via P_{scatt}, the power of the light elastically scattered from the empty trap into the immersion objective, measured behind dichroic mirror M2 (see Fig. 2). For the empty trap (*i.e.* no beads contributing to light scattering) we first obtain as a calibration $P_{scatt}(\mu W) = 17.6 \times P_{fibre}(W)$. Using this, the P_{scatt} values measured just after release give the P_{fibre} values set to just enable release. Note that P_{fibre} is not accessible to direct measurement when the fibre-waveguide alignment is preserved, which we prefer in these experiments. Using the drag force, this in turn gives the relation between P_{fibre} and F_x at release. This, when combined with the aforementioned extremum $F_x/P_{trap} = 250$ pN/W, yields $P_{trap}(mW) = 4.1 \times 10^{-2}P_{fibre}(mW)$. The prefactor 4.1×10^{-2} represents the overall transmission, including the fibre-waveguide butt coupling, the Y-junction, the waveguide bends and the straight waveguide sections. Of these the butt coupling to the diced waveguide facets by far induces the highest loss. In most of the trapping experiments P_{fibre} was 125 mW, giving $P_{trap} = 5.1$ mW (corresponding to $F_x = 1.3$ pN at release). From conventional Raman tweezers spectroscopy it is known that this power level is sufficient for Raman spectroscopy of a trapped bead.

6. Raman spectroscopy

We have performed preliminary Raman spectroscopy measurements of a single polystyrene bead optically trapped in the dual-waveguide device, using the setup of Fig. 2. Example spectra are presented in Fig. 6, for five integration times in the range 0.25-15 s. The spectra have been corrected (see below) for a separately measured background spectrum without bead in the trap. We observe that with increasing integration time distinct peaks develop in the spectra. Raman shifts of a standard spectrum of polystyrene [21], denoted by the eight dashed lines with attached shifts, agree with the positions of the measured peaks. For the peaks close to 1327 and 1450 cm^{-1} there is a small deviation, which is on the order of the spectrometer's resolution. From measurements of 11 μm beads of the same quality as the 1 μm beads with our Raman tweezers setup, in which the bead is trapped in the laser-beam focus in water without involvement of the dual-waveguide device, we find similar deviations for these two peaks from the standard spectrum. This proves that the deviation is not due to the dual-waveguide trap and suggests that sample dependent properties are involved. For the 15 s integration time we have included two traces in the figure to demonstrate the repeatability of the measurements in terms of overall spectrum shape, peak positions and intensity. Visual comparison indicates good repeatability with respect to these qualities, quantified by an average difference of 5 % as calculated from the raw data, which represent the direct measurements. We conclude from the data set that we measure the Raman spectrum of polystyrene. Above 1700 cm^{-1} and for longer integration times, some structures are present which are not polystyrene related. These could only be partly corrected by the background, due to its specific nature discussed below. We connect the structure in the range 1730-1740 cm^{-1} to Perspex, the material of the holder of the chip, of which the spectrum shows a peak at

1736 cm^{-1} [22]. The residual structures at 1900 and 1960 cm^{-1}, clearly present in both the raw spectra and the background, so far remain unidentified, although we note that they occur in the range of Raman signatures of hydrocarbon chains.
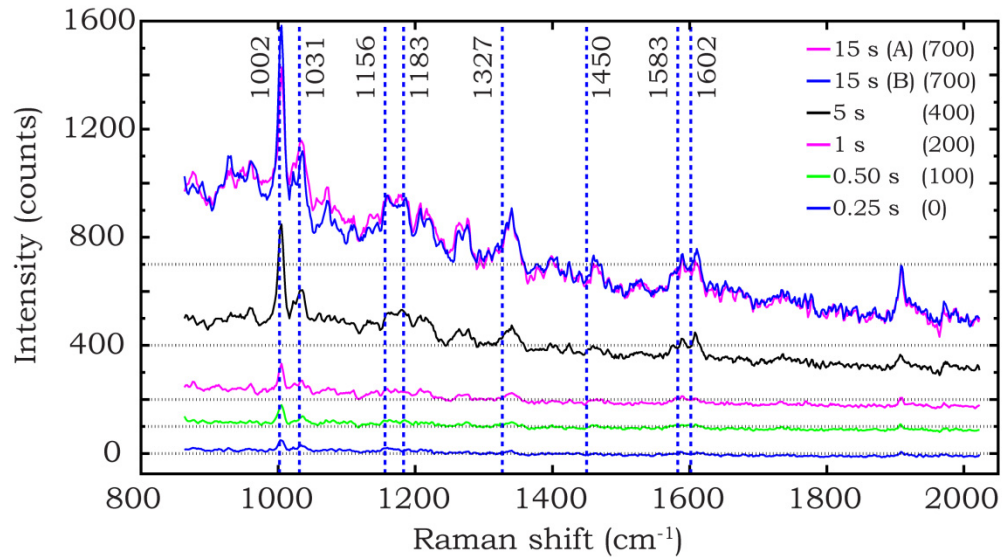

Fig. 6. Raman spectra of an optically trapped polystyrene 1 µm bead, for integration times as indicated. P_{trap} = 5.1 mW. The Raman shifts attached to the dashed lines have been taken from a standard Raman spectrum of polystyrene [21]. From the spectra a background has been subtracted and they have been slightly smoothed, as described in the text. The two 15 s spectra indicated with (A) and (B) demonstrate the repeatability of the measurements. The dotted lines are the axes of the respective spectra, showing that the intensity is negative for higher shifts as a result of the background-subtraction procedure (see text). The numbers in brackets adjacent to the integration times are the vertical offsets applied to the spectra for clarity.

The background used for correction was measured during 1 s, further conditions being similar as for the raw polystyrene spectra. Like the spectra, the background has a decaying global behavior with increasing wavenumber, without pronounced structures coinciding with Raman peaks of polystyrene. Multiplicative scaling of the background yields global decays slower than the background of the raw spectra (each having a separate scaling factor), implying that the separately measured background is an approximation of the actual background. This is not surprising, since a raw spectrum's background is affected by the presence of the bead. This serves as scatterer for all light impinging on it and thus also scatters other light than polystyrene Raman light into the objective (fluorescence light and other Raman light). Without bead this other light does not contribute to background to this degree. This is why the spectrum of the empty trap only approximates the actual background, unlike the situation of *e.g.* micro-Raman on a liquid in a cuvette. In our future research we will study the contributions to the background in more detail. We have used the background to partly remove non-polystyrene signal from the raw spectra. The criterion for the background magnitude is that its integral equals the integral of a spectrum, *i.e.* the photon count for the background is "by hand" equated to the photon count for a spectrum. Thus, the background's somewhat slower global decay is approximately equally divided over the spectrum. After background subtraction, the result was slightly smoothed using a moving average filter with a four points span, which is comparable to the resolution of the spectrometer, giving the spectra of Fig. 6. These show negative intensities for higher Raman shifts due to different decays of background and raw spectra. For the interpretation of the spectra this is irrelevant.

These results proof that this new design of the dual-waveguide trap is not only a powerful device for optical trapping but also for Raman spectroscopy of trapped particles. The Raman peaks at 1002 and 1031 cm^{-1} are still clearly measured for an integration time as short as 0.25 s, while the structures at or close to 1156, 1183, 1327, 1450 and 1602 cm^{-1} are just discernible in the spectrum for a 0.5 s integration time. This is promising for trapping and Raman spectroscopy of bio-objects such as single cells (*e.g.* bacterial spores and bacteria), which have a relatively weak Raman signal and therefore will unavoidably lead to longer integration times than used here. Such longer times are expected to be very well possible, since our Raman excitation wavelength of 785 nm is in a window of relative transparency of biological material in the near infrared portion of the spectrum (750–1200 nm) where photo-damage and heating of microorganisms and other cells are limited [11].

7. Conclusions

With a dual-*waveguide* trap based on waveguides fabricated in TripleX technology, a novel design of the dual-*beam* trap, we have optically trapped polystyrene beads from an aqueous suspension flowing through an integrated fluidic channel. A transverse trapping force as high as 1.3 pN can be exerted on a bead with a power of 5.1 mW supplied to the trap. Optical force calculations yield 0.8 pN/nm/W for the average transverse trap stiffness and 3.8 pN/nm/W for the axial stiffness of an individual local trapping potential induced by beam interference. These are high values, indicating a strong trap. Apart from particle trapping, the beams emanating from the dual waveguides are capable of inducing the Raman effect in a trapped microparticle, as we demonstrate from measured Raman spectra with a shortest integration time of 0.25 s. We suggest that III-V lasers can be heterogeneously integrated, and arrayed waveguide grating spectrometers based on TripleX technology can be homogeneously integrated with multiple dual-waveguide traps of the type we study. In this way a complete lab-on-a-chip results for in parallel trapping and Raman spectroscopy of multiple microbiological cells.